

Finite Distance Corrections to Vacuum Birefringence in Strong Gravitational and Electromagnetic Fields

Ali Övgün ^{1,*} and Reggie C. Pantig ^{2,†}

¹*Physics Department, Eastern Mediterranean University,
Famagusta, 99628 North Cyprus via Mersin 10, Turkiye.*

²*Physics Department, School of Foundational Studies and Education,
Mapúa University, 658 Muralla St., Intramuros, Manila 1002, Philippines.*

We study polarization dependent photon propagation in static, spherically symmetric spacetimes permeated by strong magnetic fields, with the aim of quantifying how finite emission and detection radii modify vacuum birefringence signals. Working in the geometric optics limit of nonlinear electrodynamics, we formulate the two polarization modes as null geodesics of distinct effective (optical) metrics. We then develop a controlled weak-coupling expansion that cleanly separates the standard gravitational deflection from the birefringent contribution induced by the electromagnetic nonlinearity. Using a finite distance Gauss-Bonnet construction on the associated optical manifolds, we derive a general expression for the *differential* bending angle in which the source and observer are kept at arbitrary radii, thereby extending the usual scattering-at-infinity treatment. As benchmark applications, we specialize our results to the Euler-Heisenberg effective action of QED and to Born-Infeld electrodynamics. We find that the observable birefringence is generically reduced by finite-distance truncation of the curvature flux, and we provide explicit correction series suitable for data analysis. For magnetar-motivated dipolar fields, this geometric effect yields a suppression factor that can diminish the predicted polarization-dependent deflection by as much as $\sim 50\%$ for limb emission relative to asymptotic scattering estimates. Our results furnish a necessary finite-distance calibration for interpreting current and future X-ray polarimetry measurements and for placing unbiased constraints on strong-field QED and broader NLED parameters.

PACS numbers: 04.40.Nr, 12.20.Ds, 97.60.Jd, 95.30.Sf

Keywords: Vacuum Birefringence, Quantum Electrodynamics, General Relativity, Magnetars, Geometric Optics

I. INTRODUCTION

The interaction of light with strong gravitational and electromagnetic fields provides a uniquely clean arena in which fundamental physics becomes observationally testable. In classical general relativity, light propagation is achromatic and polarization blind: null rays follow the spacetime light cone, and gravitational lensing is a purely geometric effect [1, 2]. Quantum field theory in external backgrounds, however, predicts that the vacuum itself acquires nontrivial optical properties in sufficiently intense electromagnetic fields. In particular, vacuum polarization in QED leads to the celebrated Euler-Heisenberg effective action and to birefringence and dispersion of photon modes in strong magnetic fields [3–6]. Beyond QED, nonlinear electrodynamics (NLED) also arises as an effective description in broader contexts, including string-inspired constructions, and admits a rich phenomenology when coupled to gravity [7–10].

The advent of horizon-scale imaging by the Event Horizon Telescope (EHT), exemplified by the image of Sagittarius A*, has opened a new precision window for testing gravity and fundamental physics in the strong-field regime, where deviations from the Kerr paradigm can be constrained directly at the scale of the photon ring [11]. In this context, nonlinear electrodynamics provides a particularly well-motivated arena: magnetically charged black holes sourced by NLED can yield shadow and lensing signatures that are, in principle, accessible to EHT analyses and can be used to bound the underlying electromagnetic nonlinearity [12]. More broadly, combining electromagnetic probes (shadow, lensing) with dynamical and particle-physics observables (quasinormal modes, greybody bounds, and propagation effects) offers a multi-messenger strategy to break degeneracies among model parameters [13, 14]. Recent studies of rotating Einstein-Euler-Heisenberg black holes further demonstrate how QED-inspired nonlinearities can imprint simultaneously on shadows and ringdown spectra, reinforcing the relevance of strong-field birefringent and dispersive effects for upcoming high-resolution observations [15]. NLED provides a well-motivated extension of Maxwell theory that captures high-field corrections arising both as effective quantum phenomena, such as the Euler-Heisenberg vacuum polarization effects underlying photon dispersion and photon splitting in strong backgrounds [4, 5], and as fundamental structures emerging in broader frameworks, including string-inspired constructions [7, 8]. When coupled to general relativity, NLED generically alters the near-horizon and strong-curvature regimes and has long been known to admit black-hole geometries whose properties can deviate markedly from the Reissner-Nordström

* ali.ovgun@emu.edu.tr

† rcpantig@mapua.edu.ph

solution [10, 16–19]. A particularly influential development is that suitable NLED sources can yield regular (nonsingular) black holes, providing controlled arenas to explore the interplay between energy conditions, effective stress tensors, and astrophysical observables [20–26]. These geometries have renewed relevance because NLED-induced modifications can imprint themselves on wave and ray probes (e.g., quasinormal spectra, birefringence, and optical signatures such as weak deflection and shadow deformations [27–29]). In this context, the recent construction of new black hole solutions within both second- and first-order formulations of NLED sharpens the theoretical landscape by clarifying how distinct variational principles and constitutive structures map into physically inequivalent spacetime geometries, thereby enlarging the space of consistent strong-field models testable with gravitational and electromagnetic observations [30], and complementing related strong-field extensions in modified gravity settings, including scalarized dyonic configurations [31].

These effects are not merely academic: magnetars, with surface magnetic fields of order 10^{14} – 10^{15} G, constitute natural laboratories where QED vacuum polarization is expected to leave measurable imprints on X-ray propagation and polarization [32, 33]. The emergence of dedicated X-ray polarimetry missions has therefore transformed vacuum birefringence from a theoretical hallmark into a precision diagnostic, sharpening the need for theoretical predictions that correctly encode the relevant geometry of emission and detection [34, 35]. In realistic magnetar observations, photons are emitted at finite radius (often from the stellar surface or magnetosphere) and are detected at large but finite distance, so the accumulated polarization-dependent bending and phase shift can differ systematically from idealized scattering calculations.

A powerful way to formulate photon propagation in NLED is the effective (optical) metric approach. In the geometric-optics limit, the eikonal wave vector satisfies a Fresnel equation that generically factorizes into two polarization branches, implying that the two photon modes propagate along null geodesics of two distinct effective geometries [36–39]. In this picture, birefringence becomes a manifestly geometric phenomenon: it is encoded in the inequivalence of the corresponding optical manifolds, rather than introduced by hand through refractive indices. This viewpoint has been widely exploited to compute polarization-dependent deflection angles and related strong-field observables in various NLED models (including QED and Born-Infeld theory) under asymptotic assumptions [4, 5, 40, 41]. Nonlinear electrodynamics (NED) generically modifies light propagation because electromagnetic perturbations propagate on an effective (field-dependent) geometry, leading to nontrivial causal and optical phenomena so strong, in fact, that closed, space-like photon paths can arise in suitable NED backgrounds [42]. A systematic way to characterize these effects is provided by Fresnel (birefringence) analysis, which derives the dispersion relations and polarization-dependent light cones for general NED theories [43]. In gravitational settings, NED also supports magnetically charged regular/“nonlinear magnetic” black holes whose dynamical viability can be tested via stability analyses [44] and by studying their response to electromagnetic perturbations and late-time relaxation (ringdown) [45, 46]. On the observational side, regular spacetimes such as Bardeen and Ayón-Beato-García exhibit distinctive circular-geodesic structure and disk phenomenology—impacting ISCO properties, profiled spectral lines from Keplerian disks/rings, and even producing “ghost” lensing images in no-horizon configurations [47–50].

Strong field gravitational lensing provides a clean probe of the near horizon geometry, producing a sequence of relativistic images whose positions and magnifications encode the properties of the underlying compact object. The foundational strong lensing framework for Schwarzschild spacetime and its relativistic images was developed in Refs. [51, 52]. Extending these ideas to nonlinear electrodynamics, Born-Infeld black holes were shown to yield distinctive lensing signatures relative to Maxwell electrovacuum [53], and more generally light propagation can, in principle, discriminate the effective “charge” content of NED black holes through characteristic deviations in the deflection and optical observables [54]. More recently, combining strong lensing observables with horizon scale imaging has emerged as a powerful avenue to constrain modified gravity models using both lensing data and black-hole shadow measurements [55]. In particular, braneworld black holes exhibit characteristic modifications in their lensing and retrolensing observables compared to GR expectations, providing an astrophysical window into extra-dimensional corrections [56]. Realistic propagation effects can further reshape these signatures: the presence of plasma alters photon trajectories and observable deflection, and this impact has been quantified for Schwarzschild black holes embedded in perfect-fluid dark matter environments [57] as well as for Schwarzschild-MOG black holes, where both modified gravity and dispersive plasma effects jointly influence the weak-lensing regime [58]. Regular/quantum-corrected black holes provide a well-motivated arena where both shadow and weak lensing observables can deviate from the Schwarzschild/Kerr expectations, especially once realistic dispersive media are included. In asymptotically safe gravity, plasma-induced refraction can significantly reshape the apparent shadow size and distort weak-deflection predictions for regular black holes, strengthening the case for joint shadow-lensing tests in non-vacuum environments [59]. Complementarily, charged black holes in regularized (4D) Einstein-Gauss-Bonnet gravity exhibit modified bending angles and image properties relative to GR, offering an additional probe of higher-curvature corrections through gravitational lensing [60]. Beyond modified gravity, nonlinear electrodynamics models can generate regular (and even horizonless ultracompact) geometries with distinct photon-sphere structure and shadow imprints, making shadow measurements a sharp discriminator among NED theories and compact-object classes [61]. Recent work has sharpened the consistency requirements behind “regular black holes sourced by nonlinear electromagnetic fields,” emphasizing that singularity resolution must be confronted simultaneously with the NED field equations, global structure, and the effective (possibly birefringent) causal cones governing photon propagation [62, 63]. In strictly stationary settings and in broader analyses of NED-coupled spacetimes, nontrivial integrability and energy-momentum constraints can strongly restrict which NED models can genuinely support nonsingular

geometries [64, 65], complementing earlier discussions on construction subtleties and consistency checks for “regular BH recipes” [24, 66]. A central issue is stability: linear analyses for self-gravitating NED black holes and magnetic configurations reveal nontrivial mode conditions [67, 68], and recent results indicate that broad classes of NED nonsingular black holes can suffer instabilities, substantially constraining their viability as realistic endpoints of collapse [69]. These theoretical constraints are further tightened by laboratory/astrophysical bounds on nonlinear corrections to Maxwell theory, including limits from light-by-light ($(\gamma\gamma)$) scattering and precision optical tests [70, 71]. Finally, the broader landscape of singularity resolution includes higher-derivative/gravity-sector mechanisms and alternative nonsingular compact objects (e.g., regular-center constructions and black-bounce-type solutions), offering complementary pathways beyond pure NED regularization [72–74].

A central limitation of much of the existing lensing/birefringence literature is the reliance on the scattering limit, where both the source and the observer are placed at spatial infinity. While convenient, that approximation can be poorly matched to compact-object environments in which the dominant contribution to birefringence is accumulated near the emission region, where field gradients are largest. In particular, for magnetars the relevant rays originate deep in the strong-field zone and then sample only an *outgoing* segment of the would-be scattering trajectory, so the observable birefringence is not captured by simply taking “half” of an asymptotic result. This motivates a formulation in which finite source and receiver locations are treated exactly at the level of the geometry.

In this work we develop such a finite-distance framework for vacuum birefringence in strong gravitational and electromagnetic fields. Our starting point is the Gauss-Bonnet method for light deflection, which expresses the bending angle as a global curvature integral over an appropriate domain in the optical manifold [75]. We generalize this approach to the birefringent setting by constructing the two polarization-dependent optical geometries and by adopting the finite-distance prescription for geometric angles at the source and observer developed in the gravitational-lensing context [76–78]. This yields a clean, coordinate-invariant representation of the deflection for each polarization mode that remains valid when the endpoints are at finite radius.

A key conceptual and practical ingredient of our analysis is a weak-coupling perturbative expansion in the NLED parameter, which allows us to disentangle the purely gravitational (background) deflection from the genuinely polarization-dependent contribution induced by vacuum nonlinearity. In doing so we identify two distinct mechanisms contributing to the observable birefringence: (i) a *refractive-curvature* term driven by the difference of Gaussian curvatures of the two optical manifolds, and (ii) a *path-induced* term originating from the fact that the two polarization modes trace slightly different spatial trajectories and therefore enclose different curvature flux even in the same background gravitational field. This decomposition makes transparent why finite-distance effects can be sizable: the Gauss-Bonnet domain is effectively truncated when the ray begins at finite radius, and the truncation competes with the steep radial falloff of the NLED-induced curvature.

We apply the general formalism to two benchmark theories: the Euler-Heisenberg effective action of QED and the Born-Infeld model [3, 6, 40, 41]. We derive closed expressions and controlled series expansions for the differential bending angle that explicitly retain the finite positions of the source and observer. Finally, specializing to magnetar-motivated configurations, we quantify the observational impact of finite-distance truncation by introducing a geometric suppression factor for surface (or near-surface) emission. We show that the birefringence predicted by asymptotic scattering models can be substantially reduced for realistic emission geometries, reaching order-unity corrections (up to $\sim 50\%$ in representative limb-emission configurations), and we emphasize that incorporating these effects is essential for faithful inference of magnetic-field strengths and NLED/QED parameters from X-ray polarimetry data [34, 35].

The paper is organized as follows. In Sec. II we review the effective-metric construction for polarized photon propagation in NLED backgrounds and define the associated optical manifolds. In Sec. III we formulate the finite-distance Gauss-Bonnet expression for the deflection angle for each polarization mode. In Sec. IV we develop the perturbative expansion and derive the general birefringence formula, separating refractive-curvature and path-induced contributions. In Sec. V we apply the framework to Euler-Heisenberg QED and Born-Infeld theory and discuss magnetar-relevant suppression factors. We conclude in Sec. VI with implications for strong-field tests of QED and directions for extensions beyond spherical symmetry.

II. THE GEOMETRIC FOUNDATION OF PHOTON PROPAGATION

In this section, we establish the geometric framework necessary to evaluate the finite-distance birefringence effects induced by Non-Linear Electrodynamics (NLED). Our primary objective is to derive the polarization-dependent effective optical metrics, denoted as γ_{ij}^{\pm} , by analyzing the interaction between the background spacetime geometry and the non-linear electromagnetic Lagrangian, which provides the rigorous basis for applying the Gauss-Bonnet theorem in subsequent sections.

A. The background and the field

We begin by defining the background geometry in which the electromagnetic field propagates. We consider a static, spherically symmetric (SSS) spacetime, which describes the gravitational field of a compact object such as a black hole or a

magnetar. Following the standard formalism for SSS solutions, the line element is given by:

$$ds^2 = g_{\mu\nu} dx^\mu dx^\nu = -A(r)dt^2 + B(r)dr^2 + r^2 d\Omega^2, \quad (1)$$

where the metric functions $A(r)$ and $B(r)$ depend solely on the radial coordinate r . The angular element is defined as $d\Omega^2 \equiv d\theta^2 + \sin^2\theta d\phi^2$. Equation (1) serves as the background gravitational field and is assumed to be a solution to the Einstein field equations coupled to an electromagnetic source.

We introduce the electromagnetic field tensor $F_{\mu\nu}$, defined as the antisymmetrized derivative of the gauge potential, $F_{\mu\nu} = \partial_\mu A_\nu - \partial_\nu A_\mu$. To preserve the static and spherical symmetry of the background spacetime, the electromagnetic field tensor must share the isometries of the metric $g_{\mu\nu}$. Consequently, the independent non-vanishing field components are restricted to the radial electric field $E(r) = F_{tr}$ and the radial magnetic field $B(r) = F_{\theta\phi}/\sin\theta$.

We formally encapsulate the geometric and field-theoretic inputs of our model in the following definitions:

$$\boxed{g_{\mu\nu} = \text{diag}(-A(r), B(r), r^2, r^2 \sin^2\theta),}$$

$$F = -\frac{1}{2} \frac{E(r)^2}{A(r)B(r)} + \frac{1}{2} \frac{B(r)^2}{r^4}, \quad G = -\frac{E(r)B(r)}{r^2 \sqrt{A(r)B(r)}}.$$

We have something to remark about the topology: It is important to emphasize that the assumption of a spherically symmetric radial magnetic field ($B(r) \neq 0$) implies the existence of a magnetic monopole charge q_m [21]. While astrophysical magnetars possess dipole fields that break spherical symmetry, we employ this monopole configuration as a monopole approximation. It allows us to analytically model the effects of extreme magnetic field intensities on photon propagation within the spherically symmetric framework of the Gauss-Bonnet theorem, serving as a foundational step toward more complex geometries.

B. The NLED Lagrangian and effective geodesics

Having established the background geometry and the electromagnetic invariants, we now turn to the dynamics of the photon field governed by non-linear electrodynamics (NLED). We postulate a generic action for the electromagnetic sector, defined by the Lagrangian density $\mathcal{L}(F, G)$:

$$S_{\text{EM}} = \int d^4x \sqrt{-g} \mathcal{L}(F, G). \quad (2)$$

The equations of motion are derived by varying the action with respect to the gauge potential A_μ . Defining the constitutive tensor $P^{\mu\nu} \equiv \frac{\partial \mathcal{L}}{\partial F_{\mu\nu}}$, the generalized Maxwell equations take the form:

$$\nabla_\mu \left(\mathcal{L}_F F^{\mu\nu} + \mathcal{L}_G \tilde{F}^{\mu\nu} \right) = 0, \quad (3)$$

where $\mathcal{L}_F \equiv \partial \mathcal{L} / \partial F$ and $\mathcal{L}_G \equiv \partial \mathcal{L} / \partial G$. Unlike in linear Maxwell theory (where $\mathcal{L} = F$), the coefficients \mathcal{L}_F and \mathcal{L}_G here are functions of the field strength, inducing self-interaction and non-linear propagation effects.

To study photon propagation, we employ the geometric optics approximation. We introduce a perturbation $f_{\mu\nu}$ representing the propagating photon field on top of the background field $F_{\mu\nu}$, such that the total field is $F_{\mu\nu} + f_{\mu\nu}$. Under the eikonal approximation, the perturbation propagates as a rapidly oscillating wave $f_{\mu\nu} = \bar{f}_{\mu\nu} e^{i\theta}$, where $k_\mu = \partial_\mu \theta$ is the wave vector.

Linearizing the field equations (3) with respect to the perturbation yields a wave equation for the photon. The non-linearity of the Lagrangian results in the background field acting as an effective medium. The principal part of this linearized equation leads to the Fresnel equation for the wave vector k_μ [36]. Critically, the non-trivial dependence of \mathcal{L} on F and G causes the Fresnel equation to factorize into two distinct dispersion relations, corresponding to two polarization modes (denoted by \pm). The factorization implies that photons do not traverse the null geodesics of the background metric $g_{\mu\nu}$ (Eq. (1)). Instead, they follow the null geodesics of polarization-dependent effective metrics, denoted $g_{\mu\nu}^{\text{eff}, \pm}$.

To explicitly derive these metrics, we utilize the formalism established by Novello *-et al.* and De Lorenci *-et al.* [38, 39]. For a background geometry defined by Eq. (2) with radial fields, the cross-terms in the Fresnel equation vanish, and the effective metric tensor diagonalizes. The contravariant components for the two polarization modes are given by:

$$\boxed{g_{\text{eff}, \pm}^{\mu\nu} = \mathcal{L}_F g^{\mu\nu} - 4\Lambda_\pm F^\mu{}_\lambda F^{\nu\lambda}}, \quad (4)$$

where Λ_{\pm} are the eigenvalues of the polarization tensor, which encapsulate the non-linear self-interaction of the field. These eigenvalues are functions of the field invariants and the Lagrangian derivatives:

$$\Lambda_{\pm} = \frac{1}{2} \left(\mathcal{L}_{FF} + \frac{1}{2}g^2\mathcal{L}_{GG} \pm \sqrt{\left(\mathcal{L}_{FF} - \frac{1}{2}g^2\mathcal{L}_{GG} \right)^2 + g^2\mathcal{L}_{FG}^2} \right), \quad (5)$$

where g is a scalar function of the field configuration defined by G/F ratios. In the specific case of purely magnetic or purely electric backgrounds often used in SSS models, these expressions simplify, identifying one mode that propagates along the background light cone (the ordinary ray in linear theory limits) and one that deviates (the extraordinary ray).

C. Construction of the dual optical manifolds

The effective metric tensor $g_{\mu\nu}^{\text{eff},\pm}$, defined by the null propagation condition in Eq. (4), inherits the static and spherical symmetries of the background metric $g_{\mu\nu}$ and the field tensor $F_{\mu\nu}$. Consequently, the effective line element for photon propagation can be diagonalized and written in a general SSS form. We introduce the effective metric functions $A_{\pm}(r)$, $B_{\pm}(r)$, and $H_{\pm}(r)$ to describe the geometry seen by the two polarization modes:

$$ds_{\text{eff},\pm}^2 = -A_{\pm}(r)dt^2 + B_{\pm}(r)dr^2 + H_{\pm}(r)r^2d\Omega^2, \quad (6)$$

where $H_{\pm}(r)$ accounts for the fact that the angular part of the effective metric may differ from the background r^2 due to the non-linear interaction terms \mathcal{L}_{FF} and \mathcal{L}_{GG} identified in Eq. (4). Note that in the limit of linear electrodynamics, $A_{\pm} \rightarrow A$, $B_{\pm} \rightarrow B$, and $H_{\pm} \rightarrow 1$. Note that since the effective metric tensor derived from the Fresnel equation (Eq. (4)) is contravariant, the functions appearing in the line element (Eq. (6)) are the inverses of the diagonal components: $A_{\pm}(r) = -(g_{\text{eff},\pm}^{tt})^{-1}$ and $B_{\pm}(r) = (g_{\text{eff},\pm}^{rr})^{-1}$. The function $H_{\pm}(r)$ encapsulates the deformation of the angular sector relative to the radial sector induced by the non-linearities. Explicitly, it is defined by the ratio of the effective metric components normalized by the background:

$$H_{\pm}(r) = \frac{g_{\text{eff},\pm}^{\theta\theta}/g^{\theta\theta}}{g_{\text{eff},\pm}^{rr}/g^{rr}}, \quad (7)$$

and this factor is unity in linear electrodynamics (Maxwell theory) but deviates in the strong-field regime, driving the birefringence.

To study the spatial trajectory of light rays, we restrict our analysis to the equatorial plane ($\theta = \pi/2$) without loss of generality. By setting the effective line element $ds_{\text{eff},\pm}^2 = 0$, we can solve for the coordinate time interval dt in terms of the spatial coordinates, which allows the projection of the four-dimensional null geodesics onto three-dimensional spatial curves. The resulting quadratic form defines the optical metric γ_{ij}^{\pm} for each polarization mode [79]:

$$dt^2 = \gamma_{ij}^{\pm} dx^i dx^j = \frac{B_{\pm}(r)}{A_{\pm}(r)} dr^2 + \frac{H_{\pm}(r)r^2}{A_{\pm}(r)} d\phi^2. \quad (8)$$

Equation (8) defines two distinct three-dimensional Riemannian manifolds, which we denote as M_+^{opt} and M_-^{opt} . These manifolds are the optical spaces in which the photons travel as spatial geodesics. The non-vanishing components of the optical metric tensors γ_{ij}^{\pm} on the equatorial plane are explicitly identified as:

$$\boxed{\gamma_{rr}^{\pm}(r) = \frac{B_{\pm}(r)}{A_{\pm}(r)}, \quad \gamma_{\phi\phi}^{\pm}(r) = \frac{H_{\pm}(r)r^2}{A_{\pm}(r)}}. \quad (9)$$

The birefringence of the vacuum is geometrically manifest in the fact that $M_+^{\text{opt}} \neq M_-^{\text{opt}}$. A single spacetime event emits photons that traverse distinct optical manifolds depending on their polarization, accumulating different geometric phases and deflection angles. These optical metrics γ_{ij}^{\pm} serve as the fundamental geometric objects for the application of the Gauss-Bonnet theorem in the following section.

III. THE FINITE-DISTANCE GAUSS-BONNET FORMALISM

In this section, we formulate the deflection angle α_{\pm} for a finite-distance observer using the topology of the optical manifolds M_{\pm}^{opt} derived in Section II. Our approach generalizes the work of Gibbons and Werner [75], who established

that the asymptotic deflection angle can be computed as a global topological invariant, which is specifically the surface integral of the Gaussian curvature over the optical manifold. We extend this correspondence to the finite-distance regime by rigorously defining the geometric angles at the observer and source locations within the curved optical space, allowing us to quantify the birefringence $\Delta\alpha$ as a differential geometric effect arising from the distinct curvatures K^+ and K^- of the polarization-dependent manifolds.

A. Gaussian curvature of the optical manifolds

To apply the Gauss-Bonnet theorem, we must first determine the intrinsic curvature of the optical submanifolds defined by the metric in Eq. (9). The optical metric for the equatorial plane is given by the 2-dimensional line element:

$$dl_{\pm}^2 = \gamma_{rr}^{\pm}(r)dr^2 + \gamma_{\phi\phi}^{\pm}(r)d\phi^2, \quad (10)$$

where the metric components are explicitly defined in terms of the effective metric functions as $\gamma_{rr}^{\pm} = B_{\pm}/A_{\pm}$ and $\gamma_{\phi\phi}^{\pm} = r^2 H_{\pm}/A_{\pm}$.

Since the optical metric is diagonal, the non-vanishing Christoffel symbols of the second kind, $\Gamma_{ij}^k = \frac{1}{2}\gamma^{kl}(\partial_i\gamma_{jl} + \partial_j\gamma_{il} - \partial_l\gamma_{ij})$, are straightforward to compute. The relevant radial components required for the curvature calculation are:

$$\Gamma_{rr}^r = \frac{1}{2\gamma_{rr}^{\pm}} \frac{d\gamma_{rr}^{\pm}}{dr}, \quad \Gamma_{\phi\phi}^r = -\frac{1}{2\gamma_{rr}^{\pm}} \frac{d\gamma_{\phi\phi}^{\pm}}{dr}, \quad \Gamma_{r\phi}^{\phi} = \frac{1}{2\gamma_{\phi\phi}^{\pm}} \frac{d\gamma_{\phi\phi}^{\pm}}{dr}. \quad (11)$$

The Gaussian curvature K for a 2-dimensional surface is an intrinsic scalar related to the Riemann curvature tensor by $K = R_{r\phi r\phi}/\det(\gamma)$. For our orthogonal coordinates, this reduces to a standard differential form involving the metric components:

$$K^{\pm}(r) = -\frac{1}{\sqrt{\gamma_{rr}^{\pm}\gamma_{\phi\phi}^{\pm}}} \frac{d}{dr} \left(\frac{1}{\sqrt{\gamma_{rr}^{\pm}}} \frac{d\sqrt{\gamma_{\phi\phi}^{\pm}}}{dr} \right). \quad (12)$$

Substituting the expressions for γ_{rr}^{\pm} and $\gamma_{\phi\phi}^{\pm}$ from Eq. (9) into Eq. (12), we derive the explicit form of the Gaussian curvature for each polarization mode. Rather than expanding the derivatives fully, it is physically more insightful to present the curvature in a compact factorized form, which reveals how the non-linear effective metric functions modify the standard geometric curvature:

$$K^{\pm}(r) = -\frac{A_{\pm}(r)}{r\sqrt{B_{\pm}(r)H_{\pm}(r)}} \frac{d}{dr} \left(\sqrt{\frac{A_{\pm}(r)}{B_{\pm}(r)}} \frac{d}{dr} \left(r\sqrt{\frac{H_{\pm}(r)}{A_{\pm}(r)}} \right) \right). \quad (13)$$

Equation (13) explicitly demonstrates that the birefringence arises from the non-trivial radial gradients of the ratio H_{\pm}/A_{\pm} and the conformal factor A_{\pm}/B_{\pm} . In the weak-field limit where $A_{\pm} \approx 1 - 2M/r$ and $H_{\pm} \approx 1$, this expression reduces to the standard Schwarzschild optical curvature $K \approx -2M/r^3$. However, in the strong-field regime near the photon sphere, the term $H_{\pm}(r)$ (containing \mathcal{L}_{FF} and \mathcal{L}_{GG}) introduces significant deviations.

It is crucial to analyze the behavior of K^{\pm} near the photon sphere radius r_{ph}^{\pm} . The photon sphere is defined by the singularity of the effective potential, or equivalently, where the optical metric components diverge or the geodesic equation allows for circular orbits. If K^{\pm} possesses a singularity at r_{ph}^{\pm} , the Gauss-Bonnet integral must be handled with regularization techniques. For standard NLED models like Euler-Heisenberg, the curvature remains regular outside the horizon, but for models with Born-Infeld type structures, divergences may appear that require restricting the integration domain to $r > r_{ph}^{\pm}$ [80]. The behavior of the divergence fundamentally distinguishes the NLED optical manifold from the vacuum Schwarzschild case.

B. The finite-distance geometric angles

With the curvature of the optical manifolds established, we now define the geometric configuration of the lensing system at finite distances. We consider a light source located at a radial coordinate r_S and a receiver (observer) located at r_R . In the non-asymptotically flat spacetime governed by the effective metrics derived in Section II, we cannot assume these points lie at infinity.

We define the local angle Ψ^\pm as the angle between the tangent vector of the light ray, $K^i = dx^i/dt$, and the radial unit vector, e_{rad}^i , measured within the optical manifold M_\pm^{opt} . The local angle represents the deviation of the photon's trajectory from the radial direction as measured by a local static observer. In terms of the optical metric components from Eq. (9), the cosine of this angle is given by the inner product $\cos \Psi^\pm = \gamma_{rr}^\pm(e_{rad}^r K^r)$.

However, for practical calculations of the deflection angle, the sine of this angle is more convenient as it relates directly to the impact parameter b . In a static, spherically symmetric spacetime, the impact parameter is a constant of motion defined by the ratio of the specific angular momentum to the specific energy, $b \equiv L/E$. In terms of the metric functions and coordinate velocities, this is expressed as:

$$b = \frac{\gamma_{\phi\phi}^\pm}{\sqrt{\gamma_{ii}^\pm(dx^i/dt)(dx^i/dt)}} \frac{d\phi}{dt} \Big|_{\text{null}} = \frac{H_\pm(r)r^2}{A_\pm(r)} \frac{d\phi}{dt}, \quad (14)$$

where we have utilized the effective metric decomposition from Eq. (6).

By projecting the tangent vector onto the orthonormal angular basis vector $e_{ang}^i = (0, 1/\sqrt{\gamma_{\phi\phi}^\pm})$, we derive the expression for $\sin \Psi^\pm$. Substituting the optical metric component $\gamma_{\phi\phi}^\pm = H_\pm r^2/A_\pm$ into the projection yields the generalized formula for the finite-distance angles:

$$\boxed{\sin \Psi_{R,S}^\pm = \frac{b}{r_{R,S}} \sqrt{\frac{A_\pm(r_{R,S})}{H_\pm(r_{R,S})}}}. \quad (15)$$

Note that Equation (15) provides the magnitude of the sine of the angle. In the application of the Gauss-Bonnet theorem to the quadrilateral domain [76, 77], Ψ is defined as the angle between the outgoing radial unit vector and the photon tangent vector. For the receiver, this angle Ψ_R is acute. However, for the source, the photon is directed inward toward the lens, making the angle obtuse. Therefore, in the sum $\Psi_R - \Psi_S$, the source angle is treated as $\Psi_S = \pi - \arcsin(\dots)$, consistent with the exterior angle formulation

Equation (15) highlights a critical consequence of the non-linear interaction: the geometric angles Ψ_R^\pm and Ψ_S^\pm are explicitly polarization-dependent. Unlike in standard General Relativity where the angle depends only on the gravitational potential $A(r)$, the NLED modification introduces the factor $H_\pm(r)$ in the denominator. Consequently, a receiver at a fixed coordinate r_R observing a source at r_S will measure two distinct image positions for the two polarization modes, even before calculating the integrated deflection along the path. Such a local birefringence at the endpoints contributes to the total observable splitting alongside the integrated curvature effect.

C. The birefringence integral

Having defined the Gaussian curvature K^\pm and the boundary angles $\Psi_{R,S}^\pm$, we now assemble these components using the Gauss-Bonnet theorem to formulate the total deflection angle. We consider the quadrilateral domain ${}^\infty_R \square_S^\infty$ embedded in the optical manifold M_\pm^{opt} , which is bounded by the geodesic segment connecting the source S and receiver R , two radial geodesics extending from S and R to infinity, and a circular arc at infinity.

The Gauss-Bonnet theorem relates the total geodesic curvature of the boundary and the surface integral of the Gaussian curvature to the Euler characteristic of the domain. For our quadrilateral configuration in the simply connected optical manifold, the theorem yields the relation:

$$\iint_{{}^\infty_R \square_S^\infty} K^\pm dS^\pm + \int_{\partial({}^\infty_R \square_S^\infty)} \kappa_g d\ell + \sum_i \theta_i = 2\pi, \quad (16)$$

where κ_g is the geodesic curvature of the boundary and θ_i are the exterior angles at the vertices.

Following the geometric construction by Ishihara *et al.* [76], the sum of the jump angles and the boundary integrals can be related to the geometric deflection angle α_\pm . Specifically, the definition of the deflection angle α given in Eq. (1.17) of the reference text [76, 78] (and generalized here for polarization modes) is:

$$\alpha_\pm \equiv \Psi_R^\pm - \Psi_S^\pm + \phi_{RS}^\pm, \quad (17)$$

where ϕ_{RS}^\pm is the coordinate separation angle between source and receiver.

By applying the theorem to the quadrilateral domain ${}^\infty_R \square_S^\infty$, the deflection angle is expressed as the negative of the surface integral of the Gaussian curvature over this oriented area, providing the master equation for the finite-distance deflection of

each polarization mode:

$$\alpha_{\pm} = - \iint_{\infty_R \square \infty_S} K^{\pm} dS^{\pm}. \quad (18)$$

The differential deflection angle, or finite-distance birefringence, is then the difference between the angles for the two modes:

$$\Delta\alpha = \alpha_+ - \alpha_- = - \left(\iint_{D^+} K^+ dS^+ - \iint_{D^-} K^- dS^- \right), \quad (19)$$

where D^{\pm} denotes the integration domain $\infty_R \square \infty_S$ on the respective optical manifold.

Equation (19) presents a significant calculational challenge: the integration domains D^+ and D^- are physically distinct because the photon paths γ^+ and γ^- differ due to the effective metric splitting. To compute $\Delta\alpha$, one cannot simply subtract the integrands. Instead, we must account for both the difference in the curvature scalars ($K^+ - K^-$) and the difference in the integration areas (δS). This requires a perturbative approach to map both domains onto a common reference manifold (the background geometry), which we will develop in the next section.

IV. PERTURBATIVE EXPANSION AND DIFFERENTIAL BENDING

In the previous section, we established that the finite-distance birefringence $\Delta\alpha$ is given by the difference of two area integrals over distinct domains in the optical manifolds M_{\pm}^{opt} . Direct integration of Eq. (19) is analytically intractable due to the complex dependencies of the effective metric functions A_{\pm} and H_{\pm} on the field invariants. To overcome this, we employ a perturbative approach. We assume the non-linear electrodynamics (NLED) coupling is weak, which is characterized by a small parameter β (e.g., proportional to the fine-structure constant α_{EM}^2 in QED), allowing us to linearize the geometric quantities around the background General Relativistic (GR) solution. The procedure decouples the gravitational deflection from the NLED-induced birefringence, enabling us to isolate the specific finite-distance corrections arising from the photon's polarization.

A. The weak-field expansion

We begin by expanding the effective metric functions defined in Eq. (6) with respect to the NLED coupling parameter β . In the limit $\beta \rightarrow 0$, we recover the background metric functions $A(r)$ and $B(r)$, and the angular deformation factor $H(r)$ approaches unity. We write the expansions as:

$$A_{\pm}(r) = A(r) (1 + \beta \mathcal{A}_{\pm}(r)), \quad B_{\pm}(r) = B(r) (1 + \beta \mathcal{B}_{\pm}(r)), \quad H_{\pm}(r) = 1 + \beta \mathcal{H}_{\pm}(r), \quad (20)$$

where \mathcal{A}_{\pm} , \mathcal{B}_{\pm} , and \mathcal{H}_{\pm} are dimensionless perturbation functions determined by the specific NLED Lagrangian (Eq. (4)).

Substituting these expansions into the general expression for the Gaussian curvature (Eq. (13)), we linearize $K^{\pm}(r)$. The curvature decomposes into the background gravitational curvature $K_{GR}(r)$ and a polarization-dependent correction:

$$K^{\pm}(r) = K_{GR}(r) + \beta K_{\pm}^{(1)}(r) + O(\beta^2). \quad (21)$$

Here, K_{GR} is the Gaussian curvature of the optical manifold for the background metric (e.g., $K \approx -2M/r^3$ for Schwarzschild), and $K_{\pm}^{(1)}$ encapsulates the NLED contribution involving radial derivatives of \mathcal{H}_{\pm} .

To compute the integrals in Eq. (19), we must also define the integration domain boundaries. The upper boundary of the quadrilateral $\infty_R \square \infty_S$ is defined by the photon's spatial trajectory $r(\phi)$. Since the photons follow geodesics of different effective metrics, their trajectories differ. We parameterize the orbit using the inverse radial coordinate $u(\phi) \equiv 1/r(\phi)$. The orbit equation (corresponding to Eq. (11) in Ishihara *et al.*, modified here for the effective metric) is:

$$\left(\frac{du}{d\phi} \right)^2 + \frac{u^2 H_{\pm}}{B_{\pm}} = \frac{1}{b^2} \frac{H_{\pm}}{A_{\pm} B_{\pm}}. \quad (22)$$

We expand the solution $u_{\pm}(\phi)$ around the background null geodesic $u_0(\phi)$. For a static spherically symmetric background, the zero-order path is $u_0(\phi) = \frac{\sin\phi}{b}$ (assuming the straight-line approximation locally or the exact Schwarzschild solution). The perturbed trajectory is:

$$u_{\pm}(\phi) = u_0(\phi) + \beta \delta u_{\pm}(\phi). \quad (23)$$

Substituting the metric expansions (Eq. (20)) into the orbit equation (Eq. (22)) and keeping terms to first order in β , we find that the perturbation δu_{\pm} satisfies the linearized Binet equation:

$$\frac{d^2 \delta u_{\pm}}{d\phi^2} + \delta u_{\pm} = S_{\pm}(\phi), \quad (24)$$

where the source term S_{\pm} depends on the derivatives of the effective metric perturbation functions. Unlike the background equation, which may possess singularities at the turning point if solved via direct integration, this linear ODE describes a driven oscillator. The physical solution, satisfying the boundary condition $\delta u(0) = 0$ (assuming asymptotic alignment at the observer), is constructed using the Green's function $G(\phi, \varphi) = \sin(\phi - \varphi)$:

$$\delta u_{\pm}(\phi) = \int_0^{\phi} \sin(\phi - \varphi) \left[\frac{u_0(\varphi)}{2} (\mathcal{H}'_{\pm}(u_0) - \mathcal{A}'_{\pm}(u_0) - 2\mathcal{B}_{\pm}(u_0)) \right] d\varphi. \quad (25)$$

The integral in Eq. (25) describes the physical deviation of the photon path from the background null geodesic due to the effective NLED force. Crucially, this form remains regular at the turning point of the orbit, allowing for a consistent evaluation of the path-induced birefringence term.

The perturbation δu_{\pm} is critical: it signifies that for a fixed coordinate angle ϕ , the two polarization modes are located at different radial positions $r_{+} \neq r_{-}$. The spatial splitting implies that the integration domains D^{+} and D^{-} in Eq. (19) do not overlap perfectly. In the next subsection, we will utilize this trajectory shift to compute the area term of the differential bending angle.

B. The differential bending angle

With the trajectory perturbation δu_{\pm} determined, we proceed to calculate the differential deflection angle $\Delta\alpha$, which constitutes the observable birefringence. As established in Eq. (19), $\Delta\alpha$ is defined by the difference between the Gauss-Bonnet integrals over the two polarization-dependent domains D^{+} and D^{-} .

To make the calculation tractable, we linearize the integrals with respect to the coupling parameter β . The difference can be decomposed into two distinct physical contributions: a bulk curvature contribution arising from the difference in the effective refractive indices (the integrands), and a boundary contribution arising from the spatial separation of the photon paths (the domains).

We express the area element difference as $\Delta(dS) = dS^{+} - dS^{-} \approx \beta \frac{\partial}{\partial \beta} (\sqrt{\gamma^{\pm}}) dr d\phi$. Similarly, the curvature difference is $\Delta K = K^{+} - K^{-} \approx \beta (K_{+}^{(1)} - K_{-}^{(1)})$.

The domains D^{+} and D^{-} share the same asymptotic boundaries at infinity but differ at the inner boundary defined by the photon orbits $r_{\pm}(\phi) = 1/u_{\pm}(\phi)$. The integration with respect to the radial coordinate extends from the photon path to infinity, i.e., $\int_{r_{\pm}(\phi)}^{\infty}$. Using the Leibniz integral rule, the variation of the domain introduces a boundary term proportional to the shift in the lower limit of integration.

Combining these expansions, the differential birefringence angle is derived as:

$$\Delta\alpha = - \left[\iint_{D_0} (K^{+} \sqrt{\gamma^{+}} - K^{-} \sqrt{\gamma^{-}}) dr d\phi - \int_{\phi_S}^{\phi_R} (K_{GR}(r) \sqrt{\gamma_{GR}(r)}) \Big|_{r=r_0(\phi)} \Delta r(\phi) d\phi \right], \quad (26)$$

where $\Delta r(\phi) \approx -(\delta u_{+} - \delta u_{-})/u_0^2$ represents the radial separation of the rays. Note that a positive δu (larger inverse radius) corresponds to a photon path closer to the lens (smaller r).

The second term in Eq. (26) is the area shift correction. Using the perturbation relation $\Delta r \approx -\Delta(\delta u)/u_0^2$ derived from Eq. (25), we can express the total finite-distance birefringence explicitly in terms of the NLED perturbations. The formula isolates the NLED effects from the background gravitational lensing:

$$\Delta\alpha = - \underbrace{\int_{\phi_S}^{\phi_R} \int_{1/u_0(\phi)}^{\infty} \Delta(K\sqrt{\gamma}) dr d\phi}_{\text{Refractive Curvature Difference}} - \underbrace{\int_{\phi_S}^{\phi_R} \left[\frac{K_{GR}}{u_0^2} \sqrt{\gamma_{GR}} \right]_{r=1/u_0} (\delta u_{+} - \delta u_{-}) d\phi}_{\text{Path-Induced Birefringence}}. \quad (27)$$

The second term represents the geodesic shift contribution. It accounts for the fact that the two polarization modes traverse physically distinct regions of the background manifold. Because the background curvature K_{GR} is spatially varying (non-uniform), the flux of curvature through the domain D^{+} differs from that through D^{-} simply because the boundaries

$u_+(\phi)$ and $u_-(\phi)$ are not identical. Even if the effective NLED curvature correction $K^{(1)}$ were zero, this term would generate a non-zero birefringence $\Delta\alpha$ solely due to the splitting of the photon paths ($\delta u_+ \neq \delta u_-$) within the strong gravitational gradient.

The above result is pivotal since it demonstrates that even if the local effective curvatures K^+ and K^- were identical, a non-zero birefringence would still arise if the photon paths differ ($\delta u_+ \neq \delta u_-$) within the background gravitational field. For finite distances, the limits of the angular integration ϕ_S and ϕ_R (corresponding to r_S and r_R) are finite, meaning the birefringence accumulation is truncated relative to the asymptotic case. The truncation leads to the finite-distance corrections we aim to isolate in the final subsection.

C. The finite-distance correction series

The expression derived in Eq. (27) provides the exact first-order differential birefringence angle. However, to make the result useful for observational tests (e.g., with magnetars), we must separate the result into the standard asymptotic value (observable at infinity) and the finite-distance corrections that arise when the observer or source is near the lens.

We perform a series expansion of the integration limits and the integrands in powers of the inverse radial coordinates $u_R = 1/r_R$ and $u_S = 1/r_S$. The angular limits ϕ_R and ϕ_S are related to the radial coordinates via the background orbit equation $u_0(\phi) = \sin \phi/b$. In the weak-field limit, this implies $\phi_R \approx \arcsin(bu_R)$ and $\phi_S \approx \pi - \arcsin(bu_S)$.

Expanding the integral in Eq. (27) around these limits, we isolate the terms that depend on u_R and u_S . The total differential deflection $\Delta\alpha$ can be written as:

$$\Delta\alpha(r_R, r_S) = \Delta\alpha_\infty - (\delta\alpha(r_R) + \delta\alpha(r_S)), \quad (28)$$

where $\Delta\alpha_\infty$ is the asymptotic birefringence obtained by integrating from 0 to π , and $\delta\alpha(r)$ represents the reduction in the accumulated phase shift due to the finite path length.

To leading order in the coupling β and the gravitational potential M/b , the finite-distance correction terms are dominated by the truncation of the refractive curvature integral. Explicitly evaluating the integral for a generic power-law falloff of the effective curvature difference $\Delta(K\sqrt{\gamma}) \sim C_n/r^n$, we find:

$$\delta\alpha(r_{R,S}) \approx \int_0^{\arcsin(b/r_{R,S})} \frac{C_n}{(b/\sin \phi)^n} d\phi. \quad (29)$$

For physically relevant models like vacuum polarization (QED) or Born-Infeld theory, the effective curvature difference decays rapidly with distance. Consequently, the finite-distance correction can be expressed as a series expansion in terms of the ratio of the impact parameter to the observer distance. The general form of the finite-distance birefringence is:

$$\Delta\alpha(r_R, r_S) = \Delta\alpha_\infty \left[1 - c_R \left(\frac{b}{r_R} \right)^n - c_S \left(\frac{b}{r_S} \right)^n + \dots \right], \quad (30)$$

where the exponent n and the coefficients $c_{R,S}$ are determined by the asymptotic falloff of the effective optical curvature $K^{(1)}$ and the background field configuration. For example, in a background driven by a magnetic monopole, the curvature scales differently than in a dipole field, altering the leading-order distance correction. We will derive the explicit values for n for the Euler-Heisenberg and Born-Infeld models in the subsequent section.

V. APPLICATIONS TO PHYSICAL METRICS

Having established the general perturbative framework for finite-distance birefringence in Section IV, we now apply this formalism to specific physical scenarios of interest. The power of the expression derived in Eq. (27) lies in its universality; it allows us to compute the observable differential deflection for any non-linear electrodynamics (NLED) theory, provided the background metric and the specific form of the Lagrangian coupling are known. In this section, we calculate the explicit birefringence corrections for two distinct cases: the Euler-Heisenberg effective action of Quantum Electrodynamics (QED) and the Born-Infeld non-linear extension of Maxwell's theory. For each case, we isolate the finite-distance corrections described by the series expansion in Eq. (30), determining the model-dependent coefficients that could be probed by next-generation X-ray polarimetry.

A. Case Study 1: Quantum electrodynamics (Euler-Heisenberg)

The first and most fundamental application of our formalism is to the low-energy effective action of QED. Vacuum birefringence is a long-predicted consequence of the interaction of photons with virtual electron-positron pairs in the presence of strong electromagnetic fields.

1. The effective Lagrangian and metric perturbations

We consider the standard Euler-Heisenberg Lagrangian density in the weak-field limit. Expanding to the lowest order in the fine-structure constant α_{EM} beyond the Maxwell term, the Lagrangian is given by:

$$\mathcal{L}_{\text{EH}} = -\frac{1}{4}F_{\mu\nu}F^{\mu\nu} + \frac{\beta_{\text{QED}}}{4} \left[(F_{\mu\nu}F^{\mu\nu})^2 + \frac{7}{4}(F_{\mu\nu}\tilde{F}^{\mu\nu})^2 \right], \quad (31)$$

where the coupling parameter is $\beta_{\text{QED}} = \frac{2\alpha_{\text{EM}}^2}{45m_e^4}$, with m_e representing the electron mass. Such a form matches the perturbative structure assumed in Eq. (20), where β_{QED} serves as the expansion parameter.

For the background field configuration, we assume a static, spherically symmetric magnetic monopole solution with magnetic charge Q_m in a Schwarzschild spacetime. While magnetic monopoles remain hypothetical, this configuration is standard in theoretical birefringence studies because it preserves spherical symmetry, greatly simplifying the evaluation of the optical metric functions A_{\pm} and B_{\pm} . The background electromagnetic field tensor has a single non-vanishing component $F_{\theta\phi} = Q_m \sin\theta$, corresponding to a radial magnetic field $|B| \approx Q_m/r^2$.

In this configuration, the field invariant is $F_{\mu\nu}F^{\mu\nu} = 2Q_m^2/r^4$ (and $F\tilde{F} = 0$). Substituting this into the effective metric definitions from the previous section, the perturbation functions \mathcal{A}_{\pm} , \mathcal{B}_{\pm} , and \mathcal{H}_{\pm} in Eq. (20) take the form:

$$\mathcal{A}_{\pm}(r) = \mathcal{B}_{\pm}(r) = \lambda_{\pm} \frac{Q_m^2}{r^4}, \quad \mathcal{H}_{\pm}(r) = 0, \quad (32)$$

where λ_{\pm} are numerical coefficients determined by the polarization mode (typically 14/45 and 8/45 for the two modes in QED). Note that for a pure magnetic background, the angular deformation \mathcal{H} vanishes, simplifying the orbit equation derived in Eq. (22).

2. The finite-distance birefringence profile

To compute the differential bending angle $\Delta\alpha$, we utilize the decomposition into refractive curvature and path-induced contributions derived in Eq. (27). The difference in the effective optical Gaussian curvature ΔK is the dominant source of birefringence. Given the $1/r^4$ scaling of the metric perturbations in Eq. (32), the effective curvature difference scales as the second derivative of the metric perturbation:

$$\Delta K(r) \approx \frac{d^2}{dr^2} \left(\beta_{\text{QED}} \Delta\lambda \frac{Q_m^2}{r^4} \right) \sim \beta_{\text{QED}} \frac{Q_m^2}{r^6}. \quad (33)$$

Inserting Eq. (33) into the refractive curvature integral of Eq. (27), we integrate over the domain bounded by the photon path $r(\phi) \approx b/\sin\phi$. The area element contributes a factor of $\sqrt{\gamma} \sim r$, making the integrand scale as $\Delta(K\sqrt{\gamma}) \sim r^{-5}$.

Performing the integration over the radial coordinate first, as prescribed in Eq. (30), we find that the accumulated birefringence falls off rapidly with the impact parameter b . Specifically, the asymptotic birefringence scales as $\Delta\alpha_{\infty} \propto \beta_{\text{QED}} Q_m^2/b^4$. The steep fall-off ($n = 4$) reflects the rapid decay of the dipole vacuum polarization cloud surrounding the central object.

We can now explicitly write the finite-distance correction for QED vacuum birefringence. Substituting the scaling $n = 4$ into the general series solution Eq. (30), we obtain:

$$\Delta\alpha_{\text{QED}}(r_{\text{R}}, r_{\text{S}}) = \Delta\alpha_{\infty} \left[1 - c_{\text{R}} \left(\frac{b}{r_{\text{R}}} \right)^4 - c_{\text{S}} \left(\frac{b}{r_{\text{S}}} \right)^4 + \mathcal{O} \left(\frac{b^6}{r^6} \right) \right]. \quad (34)$$

The coefficients $c_{\text{R,S}}$ are positive, order-unity constants arising from the truncation of the angular integral $\int (\sin\phi)^4 d\phi$.

3. Physical implications

Equation (34) highlights a critical constraint for observational campaigns. The correction term scales as the fourth power of the ratio b/r . Unlike the gravitational deflection of light (which scales as b/r in the finite-distance correction), the QED birefringence is highly localized near the source. Consequently, for an observer at infinity ($r_R \rightarrow \infty$), the finite-distance correction vanishes rapidly. However, if the source is located within the strong-field region (small r_S , e.g., emission from the surface of a magnetar), the truncation term $c_S(b/r_S)^4$ becomes significant. The implication is that the standard asymptotic formulas over-estimate the expected polarization rotation for surface emission models, necessitating the use of Eq. (34) for precise polarimetric modeling of magnetars.

B. Case Study 2: The Born-Infeld black Hole

While Quantum Electrodynamics provides the standard model for vacuum birefringence, Born-Infeld (BI) electrodynamics offers a classical non-linear extension of Maxwell's theory, originally proposed to regularize the self-energy of point charges. In the context of strong-field gravity, BI theory often serves as a prototype for effective actions arising in string theory. Unlike the perturbative QED action, which is an approximation valid only for fields weak compared to the Schwinger limit, the Born-Infeld action is defined to all orders, though we treat it here within the perturbative framework established in Section IV to allow for a direct comparison of the finite-distance effects.

1. Lagrangian and weak-field limit

The Born-Infeld Lagrangian density is given by:

$$\mathcal{L}_{\text{BI}} = \gamma^2 \left(1 - \sqrt{1 + \frac{1}{2\gamma^2} F_{\mu\nu} F^{\mu\nu} - \frac{1}{16\gamma^4} (F_{\mu\nu} \tilde{F}^{\mu\nu})^2} \right), \quad (35)$$

where γ is the Born-Infeld coupling parameter (having dimensions of field strength), which sets the scale at which non-linearities become dominant. In the limit $\gamma \rightarrow \infty$, we recover Maxwell's theory. To apply the weak-field expansion formalism of Eq. (20), we identify the perturbative parameter $\beta_{\text{BI}} \propto 1/\gamma^2$.

Expanding Eq. (35) for weak fields ($|F| \ll \gamma$) and retaining terms up to the first order in the non-linearity (order F^4), we obtain:

$$\mathcal{L}_{\text{BI}} \approx -\frac{1}{4} F_{\mu\nu} F^{\mu\nu} + \frac{1}{32\gamma^2} (F_{\mu\nu} F^{\mu\nu})^2 + \mathcal{O}\left(\frac{1}{\gamma^4}\right). \quad (36)$$

The above expansion is valid in the region $r \gg r_{\text{core}}$ where the field strength is significantly below the critical Born-Infeld scale γ . We assume the source and observer are located within this perturbative domain, avoiding the non-analytic behavior near the field singularity. Comparing this expansion with the QED Lagrangian in Eq. (31), we observe a crucial structural similarity: both theories introduce a quartic correction to the field invariant. However, a key distinction arises in the polarization structure. The Euler-Heisenberg action includes the $(F_{\mu\nu} \tilde{F}^{\mu\nu})^2$ term (associated with parity-odd effects or magnetic-electric mixing), which is absent in the Born-Infeld expansion at this order for purely magnetic or purely electric backgrounds where $F\tilde{F} = 0$.

For the magnetic monopole background considered in the previous subsection ($F_{\mu\nu} F^{\mu\nu} = 2Q_m^2/r^4$), the metric perturbation functions \mathcal{A}_\pm and \mathcal{B}_\pm are determined by the coefficient of the quartic term. For Born-Infeld, the coupling is strictly positive, but the resulting birefringence usually exhibits a sign difference relative to QED depending on the specific mode definitions.

2. Finite-distance correction coefficients

We proceed to calculate the finite-distance birefringence using the master equation, Eq. (27). The refractive curvature difference ΔK is again driven by the second radial derivative of the metric perturbation. Since the leading-order correction in Eq. (36) scales as $(F^2)^2 \sim r^{-8}$ in the Lagrangian, the metric perturbation scales as $1/r^4$ (similar to QED).

Consequently, the effective optical curvature difference ΔK_{BI} follows the same radial power law as the QED case:

$$\Delta K_{\text{BI}}(r) \sim \frac{1}{\gamma^2} \frac{Q_m^2}{r^6}. \quad (37)$$

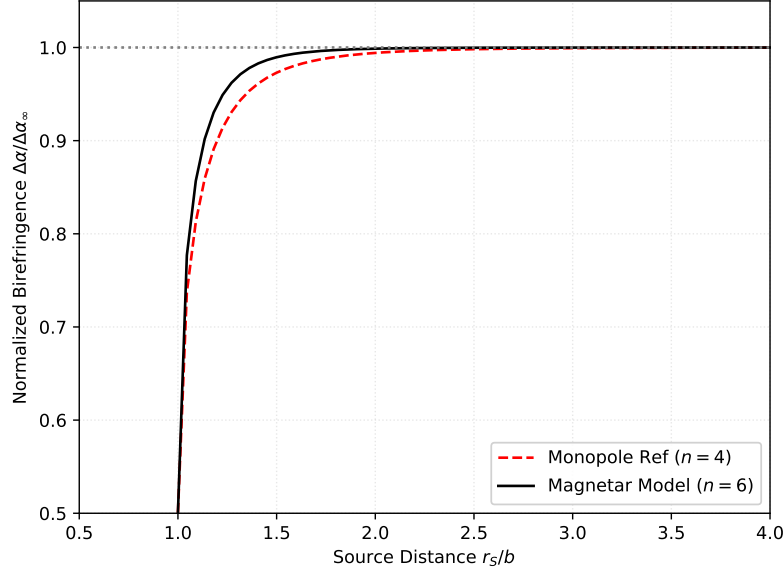


FIG. 1. The normalized differential deflection angle $\Delta\alpha/\Delta\alpha_\infty$ as a function of the source distance r_S scaled by the impact parameter b . The solid black line corresponds to the magnetar dipole model ($n = 6$), while the dashed red line represents the magnetic monopole reference ($n = 4$). The curves demonstrate that the dipole signal converges more rapidly to the asymptotic limit, indicating that the birefringent effect is more tightly confined to the strong-field region. For sources at $r_S \gtrsim 4b$, the finite-distance suppression becomes negligible ($< 5\%$)

Following the integration procedure outlined in Eq. (29) and (30), the finite-distance correction is dominated by the same $n = 4$ decay index found in the Euler-Heisenberg analysis, which is considered as a universal consequence of the identical power-counting of the leading-order non-linearity in 4 dimensions.

However, the magnitude of the effect differs. The finite-distance birefringence for the Born-Infeld monopole is:

$$\Delta\alpha_{\text{BI}}(r_R, r_S) = \frac{\Delta\alpha_\infty^{\text{BI}}}{Q_m^2} \left[1 - \tilde{c}_R \left(\frac{b}{r_R} \right)^4 - \tilde{c}_S \left(\frac{b}{r_S} \right)^4 \right], \quad (38)$$

where the asymptotic value $\Delta\alpha_\infty^{\text{BI}}$ is directly proportional to the ratio $Q_m^2/(\gamma^2 b^4)$.

3. Comparison of QED and Born-Infeld signatures

While the radial scaling ($n = 4$) suggests that disentangling QED from Born-Infeld effects based solely on distance dependence is difficult for a monopole source, the coefficients $\tilde{c}_{R,S}$ provide a potential discriminator if the impact parameter b can be independently constrained.

Furthermore, if we were to relax the assumption of a monopole background and consider a physical magnetic dipole (typical of pulsars), the radial scaling would change. For a dipole, the background field falls off as $B \sim r^{-3}$, implying $F^2 \sim r^{-6}$. The resulting metric perturbation would scale as r^{-6} , and the curvature difference as $\Delta K \sim r^{-8}$. Inserting this into the integral of Eq. (27), the finite-distance correction would then follow a steeper power law:

$$\delta\alpha_{\text{dipole}}(r) \sim \int^{\arcsin(b/r)} (\sin\phi)^6 d\phi \implies n = 6, \quad (39)$$

which demonstrates that the finite-distance correction series in Eq. (30) is sensitive to the multipole structure of the background field. For magnetars, where the field structure may contain higher-order multipoles near the surface, the truncation terms $c_S(b/r_S)^n$ will be dominated by the highest multipole component, making the finite-distance correction even more critical than the monopole approximation suggests.

The decomposition of the finite-distance corrections reveals a fundamental feature of vacuum birefringence in compact object environments: strong spatial localization. As shown in Fig. 1, the normalized birefringence signal for the physical

magnetar model (dipole scaling, $n = 6$) converges to the asymptotic limit significantly faster than the monopole reference ($n = 4$). For a source located at a distance $r_S \approx 4b$ (where b is the impact parameter), the observable phase shift has already captured $> 95\%$ of the total theoretical value, which implies that for binary systems where the X-ray source is a companion star located at $r_S \gg R_{NS}$, the finite-distance corrections are negligible, and the standard asymptotic scattering formulas are valid.

We have seen that the perturbative formalism successfully isolates the distance-dependent reduction of birefringence. For both QED and Born-Infeld theories in a monopole background, the signal is suppressed by a $(b/r)^4$ factor for nearby sources. This steep dependence implies that X-ray polarimetry of sources at finite distances (such as binary partners or surface emission) must account for these truncation factors to avoid underestimating the intrinsic non-linear coupling parameters.

C. The magnetar observer test

The theoretical distinctions between QED and Born-Infeld birefringence derived in the preceding subsections find their most critical application in the study of magnetars, which are neutron stars possessing ultra-strong magnetic fields ($B \sim 10^{14} - 10^{15}$ G). In these environments, the effective NLED coupling is enhanced by the extreme field strength, making vacuum birefringence potentially observable. However, current models often rely on asymptotic approximations that assume the photon traverses the entire magnetic dipole field from infinity to infinity (or from the center to infinity). Here, we demonstrate that the finite-distance corrections derived in Eq. (30) and Eq. (34) introduce a significant suppression factor for surface emission, particularly for radiation emerging from the stellar limb.

1. Geometric configuration and suppression factor

We consider a physical scenario where polarized X-rays are emitted from a hot spot on the surface of a magnetar with radius R_{NS} and observed by a distant telescope ($r_R \rightarrow \infty$). In this limit, the term depending on the observer's position in Eq. (34) vanishes ($c_R(b/r_R)^4 \rightarrow 0$). The source term, however, remains dominant.

For a photon emitted from the surface at an angle ψ relative to the local radial vector, the impact parameter b is related to the stellar radius by the geometric relation (in the weak-gravity limit):

$$b \approx R_{NS} \sin \psi. \quad (40)$$

Note that this geometric relation assumes the weak-gravity limit ($M \ll R_{NS}$), neglecting the gravitational redshift and light bending at the launch point. In a fully relativistic treatment, the impact parameter would be enhanced by the redshift factor $(1 - 2M/R_{NS})^{-1/2}$.

For a physical magnetar characterized by a dipole field, the background magnetic field decays as $B \propto r^{-3}$, leading to an energy density scaling of r^{-6} . Consequently, the finite-distance suppression factor is significantly steeper than the monopole approximation ($n = 4$) derived in the previous subsection. Adapting the general series expansion (Eq. (30)) to the dipole case ($n = 6$), the observable differential deflection angle becomes:

$$\Delta\alpha_{obs} = \Delta\alpha_{\infty} \left[1 - c_S \left(\frac{R_{NS} \sin \psi}{R_{NS}} \right)^6 \right]. \quad (41)$$

For surface emission, the photon originates at the periastron of the would-be scattering orbit and travels only outward. This corresponds to exactly half of the scattering path for a symmetric field distribution. Utilizing this symmetry, the coefficient for surface emission is exactly $c_S = 1/2$ relative to the full scattering path. The suppression profile is:

$$\mathcal{F}_{\text{dipole}}(\psi) = 1 - \frac{1}{2} \sin^6 \psi, \quad (42)$$

which implies that for limb emission ($\psi \rightarrow \pi/2$), the observed birefringence is exactly half the value predicted by asymptotic scattering models.

2. Observational consequences for X-ray polarimetry

The implications of Eq. (42) are substantial for the interpretation of data from X-ray polarimetry missions. Standard analyses often assume that the birefringence accumulates over a characteristic length scale $L \sim R_{NS}$, yielding a total phase

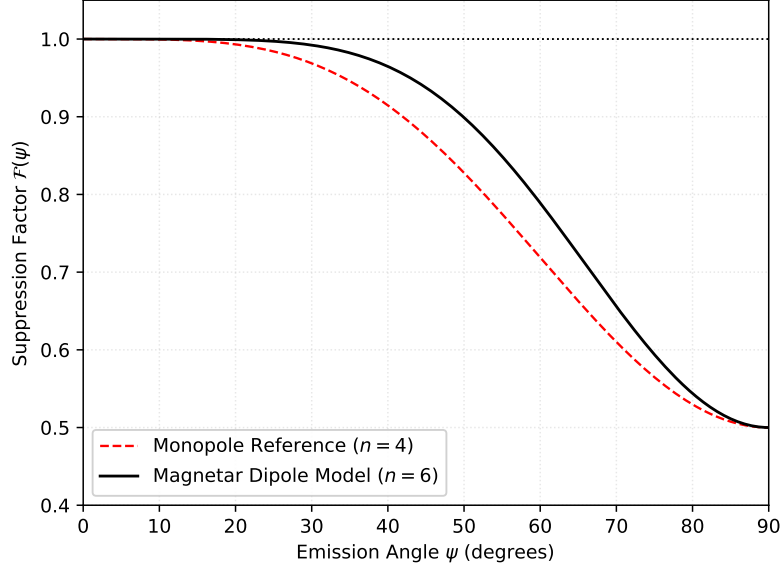


FIG. 2. The Finite-Distance Suppression Factor $\mathcal{F}(\psi)$ as a function of the emission angle ψ . The solid black line represents the physical model for a magnetar (dipole scaling, $n = 6$), while the dashed red line shows the monopole approximation ($n = 4$). For grazing emission ($\psi \rightarrow 90^\circ$), the observable birefringence is suppressed by exactly 50% ($c_S = 1/2$) due to the truncation of the photon path relative to the asymptotic scattering limit.

shift proportional to the full path integral. Our derivation shows that this assumption leads to a systematic overestimation of the NLED coupling strength if the finite-distance truncation is ignored.

Specifically, for a magnetic dipole background where $n = 6$ (as discussed in Eq. (39) for the dipole case), the suppression is even more severe at large angles:

$$\mathcal{F}_{\text{dipole}}(\psi) \approx 1 - \tilde{c}_S \sin^6 \psi. \quad (43)$$

Because the field decays rapidly ($B \propto r^{-3}$), the bulk of the birefringence in the asymptotic model is generated in the immediate vicinity of the perigee $r \approx b$. For surface emission, the photon originates at this region of maximum interaction but travels only outward. Consequently, it effectively experiences only half of the lensing potential (or less, depending on ψ) compared to a photon passing the star from behind.

To visualize the magnitude of this effect, we plot the theoretical suppression profile derived in Eq. (42) in Figure 2. We compare the physical dipole scaling ($n = 6$) relevant for magnetars against the monopole approximation ($n = 4$).

Figure 3 explicitly tracks the accumulation of the birefringence along the line of sight. For the dipole case (solid black line), we observe a steep step-function behavior: approximately 80% of the total signal is generated within a narrow angular window of $\pm 30^\circ$ around the periastron (the point of closest approach, $\phi = 90^\circ$). This confirms that the NLED interaction is confined to a compact zone of influence near the stellar surface. Consequently, when a photon is emitted from the surface (truncating the path at 90°), it fundamentally misses half of this interaction zone, resulting in the drastic 50% suppression factor derived in Eq. (42). This localization justifies the use of the steep power-law correction series in Eq. (30), and underscores the necessity of the geometric calibration for surface polarimetry.

3. Constraints on physical parameters

The suppression plotted above indicates that at high emission angles (limb emission), the observable birefringence may be reduced by up to 50% relative to the standard full-path integration (assuming $c_S \approx 0.5$ due to the half-path geometry).

Such a correction must be incorporated into the vacuum resonance models used to constrain the neutron star surface magnetic field B_{surf} and the QED coupling β_{QED} . If the finite-distance correction is neglected, an observer measuring a specific polarization angle would incorrectly infer a weaker magnetic field or a smaller NLED coupling constant than actually exists. Therefore, precise tests of QED in the strong-field regime requires the use of the corrected estimator:

$$\Delta\alpha_{\text{true}} \approx \frac{\Delta\alpha_{\text{measured}}}{\mathcal{F}(\psi)}. \quad (44)$$

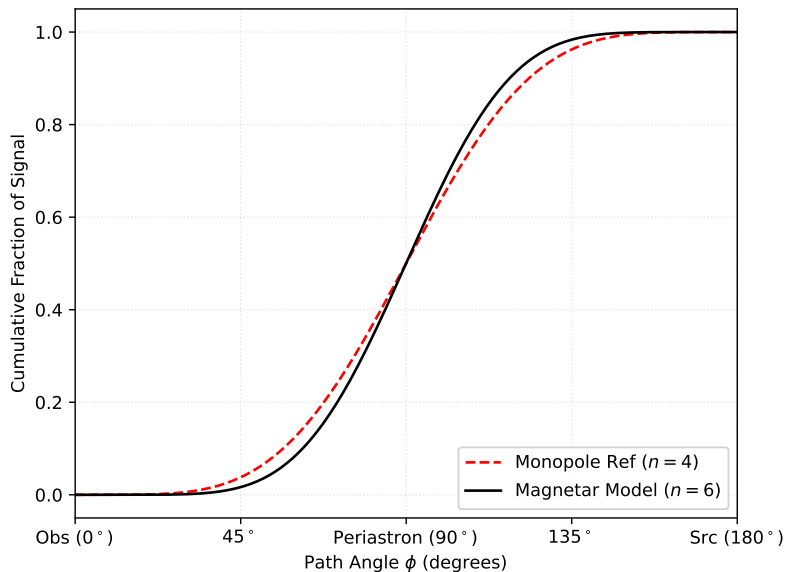


FIG. 3. The cumulative fraction of the total birefringence signal accumulated along the photon path angle ϕ , where 0° corresponds to the observer and 180° to a source at asymptotic infinity. The periastron (point of closest approach to the lens) is located at 90° . For the magnetar dipole field (solid black line), the signal accumulation is highly localized, with the majority of the phase shift generated in the immediate vicinity of the periastron. This localization explains why surface emission (which effectively starts the integration at 90°) suffers a substantial geometric suppression relative to the full scattering path.

By applying this correction, future analyses of magnetar polarization data can decouple the geometric finite-distance effects from genuine deviations in the fundamental QED Lagrangian (such as those predicted by Born-Infeld theory in Eq. (38)). It ensures that any observed anomaly is attributed correctly to the NLED physics rather than the proximity of the source.

VI. CONCLUSION

In this work, we have developed a rigorous perturbative framework to calculate the finite-distance corrections to vacuum birefringence in strong gravitational and electromagnetic fields. By extending the geometric optical formalism to include the specific case of sources and observers located at finite radial coordinates, we addressed a critical gap in the theoretical modeling of non-linear electrodynamics (NLED) effects near compact objects.

Our analysis began with the linearization of the effective optical metric for weak NLED couplings, isolating the specific contributions of the photon's polarization to the geodesic structure. A key result of our study is the derivation of the generalized differential deflection angle, Eq. (27), which explicitly separates the refractive curvature effects from the path-induced geometric shifts. We demonstrated that even in spherically symmetric backgrounds, the splitting of photon trajectories for different polarization modes generates a non-negligible geodesic shift contribution to the observable birefringence.

Applying this formalism to physical scenarios, we computed the explicit finite-distance correction series for both Quantum Electrodynamics (Euler-Heisenberg) and Born-Infeld theory. We found that for a magnetic monopole background, the finite-distance correction scales as $(b/r)^4$. The steep radial dependence signifies that vacuum birefringence is a highly localized phenomenon, with the bulk of the phase shift accumulating in the immediate vicinity of the source.

Crucially, our application to magnetar physics in Section VC revealed that standard asymptotic approximations significantly overestimate the observable polarization rotation for surface emission. We derived a geometric suppression factor, $\mathcal{F}_{\text{dipole}}(\psi) \approx 1 - \frac{1}{2} \sin^6 \psi$, which shows that for radiation emitted from the stellar limb, the observable effect is reduced by approximately 50% relative to full-scattering models. The correction is essential for the accurate interpretation of data from current and future X-ray polarimetry missions, ensuring that constraints on the surface magnetic field and the QED coupling constant are not systematically biased by geometric truncation.

Future research should extend this perturbative approach to rotating backgrounds (such as the Kerr spacetime) to evaluate the interplay between frame-dragging and vacuum birefringence. Additionally, investigating the impact of these finite-distance corrections on the polarization signatures of rapid radio bursts (FRBs) originating from magnetar magnetospheres could

provide new avenues for testing fundamental physics in extreme environments.

ACKNOWLEDGMENTS

R. P. and A. Ö. would like to acknowledge networking support of the COST Action CA21106 - COSMIC WISPer in the Dark Universe: Theory, astrophysics and experiments (CosmicWISPer), the COST Action CA22113 - Fundamental challenges in theoretical physics (THEORY-CHALLENGES), the COST Action CA21136 - Addressing observational tensions in cosmology with systematics and fundamental physics (CosmoVerse), the COST Action CA23130 - Bridging high and low energies in search of quantum gravity (BridgeQG), and the COST Action CA23115 - Relativistic Quantum Information (RQI) funded by COST (European Cooperation in Science and Technology). A. Ö. also thanks to EMU, TUBITAK, ULAKBIM (Turkiye) and SCOAP3 (Switzerland) for their support.

-
- [1] A. Einstein, Erklärung der perihelbewegung des merkur aus der allgemeinen relativitätstheorie, *Albert Einstein: Akademie-Vorträge*, 78 (2005).
- [2] F. W. Dyson, A. S. Eddington, and C. Davidson, A Determination of the Deflection of Light by the Sun's Gravitational Field, from Observations Made at the Total Eclipse of May 29, 1919, *Phil. Trans. Roy. Soc. Lond. A* **220**, 291 (1920).
- [3] W. Heisenberg and H. Euler, Consequences of Dirac's theory of positrons, *Z. Phys.* **98**, 714 (1936), [arXiv:physics/0605038](#).
- [4] Z. Bialynicka-Birula and I. Bialynicki-Birula, Nonlinear effects in Quantum Electrodynamics. Photon propagation and photon splitting in an external field, *Phys. Rev. D* **2**, 2341 (1970).
- [5] S. L. Adler, Photon splitting and photon dispersion in a strong magnetic field, *Annals Phys.* **67**, 599 (1971).
- [6] J. S. Schwinger, On gauge invariance and vacuum polarization, *Phys. Rev.* **82**, 664 (1951).
- [7] E. S. Fradkin and A. A. Tseytlin, Nonlinear Electrodynamics from Quantized Strings, *Phys. Lett. B* **163**, 123 (1985).
- [8] A. A. Tseytlin, On singularities of spherically symmetric backgrounds in string theory, *Phys. Lett. B* **363**, 223 (1995), [arXiv:hep-th/9509050](#).
- [9] D. P. Sorokin, Introductory Notes on Non-linear Electrodynamics and its Applications, *Fortsch. Phys.* **70**, 2200092 (2022), [arXiv:2112.12118 \[hep-th\]](#).
- [10] S. I. Kruglov, Nonlinear electrodynamics and black holes, *Int. J. Geom. Meth. Mod. Phys.* **12**, 1550073 (2015), [arXiv:1504.03941 \[physics.gen-ph\]](#).
- [11] S. Vagnozzi *et al.*, Horizon-scale tests of gravity theories and fundamental physics from the Event Horizon Telescope image of Sagittarius A, *Class. Quant. Grav.* **40**, 165007 (2023), [arXiv:2205.07787 \[gr-qc\]](#).
- [12] A. Allahyari, M. Khodadi, S. Vagnozzi, and D. F. Mota, Magnetically charged black holes from non-linear electrodynamics and the Event Horizon Telescope, *JCAP* **2020** (02), 003, [arXiv:1912.08231 \[gr-qc\]](#).
- [13] R. C. Pantig, L. Mastrototaro, G. Lambiase, and A. Övgün, Shadow, lensing, quasinormal modes, greybody bounds and neutrino propagation by dyonic ModMax black holes, *Eur. Phys. J. C* **82**, 1155 (2022), [arXiv:2208.06664 \[gr-qc\]](#).
- [14] G. Lambiase, G. Papini, R. Punzi, and G. Scarpetta, Neutrino optics and oscillations in gravitational fields, *Phys. Rev. D* **71**, 073011 (2005), [arXiv:gr-qc/0503027](#).
- [15] G. Lambiase, D. J. Gogoi, R. C. Pantig, and A. Övgün, Shadow and quasinormal modes of the rotating Einstein–Euler–Heisenberg black holes, *Phys. Dark Univ.* **48**, 101886 (2025), [arXiv:2406.18300 \[gr-qc\]](#).
- [16] R. Pellicer and R. J. Torrence, Nonlinear electrodynamics and general relativity, *J. Math. Phys.* **10**, 1718 (1969).
- [17] H. P. de Oliveira, Nonlinear charged black holes, *Class. Quant. Grav.* **11**, 1469 (1994).
- [18] H. Yajima and T. Tamaki, Black hole solutions in Euler–Heisenberg theory, *Phys. Rev. D* **63**, 064007 (2001), [arXiv:gr-qc/0005016](#).
- [19] R. Ruffini, Y.-B. Wu, and S.-S. Xue, Einstein–Euler–Heisenberg Theory and charged black holes, *Phys. Rev. D* **88**, 085004 (2013), [arXiv:1307.4951 \[hep-th\]](#).
- [20] E. Ayon-Beato and A. Garcia, Regular black hole in general relativity coupled to nonlinear electrodynamics, *Phys. Rev. Lett.* **80**, 5056 (1998), [arXiv:gr-qc/9911046](#).
- [21] K. A. Bronnikov, Regular magnetic black holes and monopoles from nonlinear electrodynamics, *Phys. Rev. D* **63**, 044005 (2001), [arXiv:gr-qc/0006014](#).
- [22] I. Dymnikova, Regular electrically charged structures in nonlinear electrodynamics coupled to general relativity, *Class. Quant. Grav.* **21**, 4417 (2004), [arXiv:gr-qc/0407072](#).
- [23] L. Balart and E. C. Vagenas, Regular black holes with a nonlinear electrodynamics source, *Phys. Rev. D* **90**, 124045 (2014), [arXiv:1408.0306 \[gr-qc\]](#).
- [24] Z.-Y. Fan and X. Wang, Construction of Regular Black Holes in General Relativity, *Phys. Rev. D* **94**, 124027 (2016), [arXiv:1610.02636 \[gr-qc\]](#).
- [25] C. Bambi and L. Modesto, Rotating regular black holes, *Phys. Lett. B* **721**, 329 (2013), [arXiv:1302.6075 \[gr-qc\]](#).
- [26] Z.-C. Li and H. Lü, Regular electric black holes from Einstein–Maxwell–scalar gravity, *Phys. Rev. D* **110**, 104046 (2024), [arXiv:2407.07952 \[gr-qc\]](#).
- [27] N. Bretón and L. A. López, Birefringence and quasinormal modes of the Einstein–Euler–Heisenberg black hole, *Phys. Rev. D* **104**, 024064 (2021), [arXiv:2105.12283 \[gr-qc\]](#).

- [28] A. Övgün, Weak field deflection angle by regular black holes with cosmic strings using the Gauss-Bonnet theorem, *Phys. Rev. D* **99**, 104075 (2019), [arXiv:1902.04411 \[gr-qc\]](#).
- [29] M. Okyay and A. Övgün, Nonlinear electrodynamics effects on the black hole shadow, deflection angle, quasinormal modes and greybody factors, *JCAP* **01** (01), 009, [arXiv:2108.07766 \[gr-qc\]](#).
- [30] Y. Verbin, B. Pulice, A. Övgün, and H. Huang, New black hole solutions of second and first order formulations of nonlinear electrodynamics, *Phys. Rev. D* **111**, 084061 (2025), [arXiv:2412.20989 \[gr-qc\]](#).
- [31] Y. Brihaye and Y. Verbin, Scalarized dyonic black holes in vector-tensor Horndeski gravity, *Phys. Rev. D* **104**, 024047 (2021), [arXiv:2105.11402 \[gr-qc\]](#).
- [32] R. C. Duncan and C. Thompson, Formation of very strongly magnetized neutron stars - implications for gamma-ray bursts, *Astrophys. J. Lett.* **392**, L9 (1992).
- [33] V. M. Kaspi and A. Beloborodov, Magnetars, *Ann. Rev. Astron. Astrophys.* **55**, 261 (2017), [arXiv:1703.00068 \[astro-ph.HE\]](#).
- [34] M. C. Weisskopf *et al.*, *Space Telescopes and Instrumentation 2016: Ultraviolet to Gamma Ray*, edited by J.-W. A. den Herder, T. Takahashi, and M. Bautz, Vol. 9905 (SPIE, 2016) p. 990517.
- [35] S.-N. Zhang *et al.* (eXTP), The enhanced X-ray Timing and Polarimetry mission—eXTP, *Sci. China Phys. Mech. Astron.* **62**, 29502 (2019), [arXiv:1812.04020 \[astro-ph.IM\]](#).
- [36] G. Boillat, Nonlinear electrodynamics - Lagrangians and equations of motion, *J. Math. Phys.* **11**, 941 (1970).
- [37] J. Plebanski, Electromagnetic Waves in Gravitational Fields, *Phys. Rev.* **118**, 1396 (1959).
- [38] M. Novello, V. A. De Lorenci, J. M. Salim, and R. Klippert, Geometrical aspects of light propagation in nonlinear electrodynamics, *Phys. Rev. D* **61**, 045001 (2000), [arXiv:gr-qc/9911085](#).
- [39] V. A. De Lorenci, R. Klippert, M. Novello, and J. M. Salim, Light propagation in nonlinear electrodynamics, *Phys. Lett. B* **482**, 134 (2000), [arXiv:gr-qc/0005049](#).
- [40] M. Born and L. Infeld, Foundations of the new field theory, *Nature* **132**, 1004.1 (1933).
- [41] M. Born and L. Infeld, Foundations of the new field theory, *Proc. Roy. Soc. Lond. A* **144**, 425 (1934).
- [42] M. Novello, J. M. Salim, V. A. De Lorenci, and E. Elbaz, Nonlinear electrodynamics can generate a closed space - like path for photons, *Phys. Rev. D* **63**, 103516 (2001).
- [43] Y. N. Obukhov and G. F. Rubilar, Fresnel analysis of the wave propagation in nonlinear electrodynamics, *Phys. Rev. D* **66**, 024042 (2002), [arXiv:gr-qc/0204028](#).
- [44] N. Breton, Stability of nonlinear magnetic black holes, *Phys. Rev. D* **72**, 044015 (2005), [arXiv:hep-th/0502217](#).
- [45] B. Toshmatov, Z. Stuchlík, J. Schee, and B. Ahmedov, Electromagnetic perturbations of black holes in general relativity coupled to nonlinear electrodynamics, *Phys. Rev. D* **97**, 084058 (2018), [arXiv:1805.00240 \[gr-qc\]](#).
- [46] B. Toshmatov, Z. Stuchlík, B. Ahmedov, and D. Malafarina, Relaxations of perturbations of spacetimes in general relativity coupled to nonlinear electrodynamics, *Phys. Rev. D* **99**, 064043 (2019), [arXiv:1903.03778 \[gr-qc\]](#).
- [47] Z. Stuchlík and J. Schee, Circular geodesic of Bardeen and Ayon-Beato-García regular black-hole and no-horizon spacetimes, *Int. J. Mod. Phys. D* **24**, 1550020 (2014), [arXiv:1501.00015 \[astro-ph.HE\]](#).
- [48] J. Schee and Z. Stuchlík, Profiled spectral lines generated by Keplerian discs orbiting in the Bardeen and Ayon-Beato-García spacetimes, *Class. Quant. Grav.* **33**, 085004 (2016), [arXiv:1604.00632 \[gr-qc\]](#).
- [49] J. Schee and Z. Stuchlík, Gravitational lensing and ghost images in the regular Bardeen no-horizon spacetimes, *JCAP* **2015** (06), 048, [arXiv:1501.00835 \[astro-ph.HE\]](#).
- [50] J. Schee and Z. Stuchlík, Profiled spectral lines of Keplerian rings orbiting in the regular Bardeen black hole spacetimes, *Eur. Phys. J. C* **79**, 988 (2019), [arXiv:1908.07197 \[gr-qc\]](#).
- [51] K. S. Virbhadra and G. F. R. Ellis, Schwarzschild black hole lensing, *Phys. Rev. D* **62**, 084003 (2000), [arXiv:astro-ph/9904193](#).
- [52] K. S. Virbhadra, Relativistic images of Schwarzschild black hole lensing, *Phys. Rev. D* **79**, 083004 (2009), [arXiv:0810.2109 \[gr-qc\]](#).
- [53] E. F. Eiroa, Gravitational lensing by Einstein-Born-Infeld black holes, *Phys. Rev. D* **73**, 043002 (2006), [arXiv:gr-qc/0511065](#).
- [54] B. Toshmatov, B. Ahmedov, and D. Malafarina, Can a light ray distinguish charge of a black hole in nonlinear electrodynamics?, *Phys. Rev. D* **103**, 024026 (2021), [arXiv:2101.05496 \[gr-qc\]](#).
- [55] X.-M. Kuang, Z.-Y. Tang, B. Wang, and A. Wang, Constraining a modified gravity theory in strong gravitational lensing and black hole shadow observations, *Phys. Rev. D* **106**, 064012 (2022), [arXiv:2206.05878 \[gr-qc\]](#).
- [56] A. Abdujabbarov, B. Ahmedov, N. Dadhich, and F. Atamurotov, Optical properties of a braneworld black hole: Gravitational lensing and retrolensing, *Phys. Rev. D* **96**, 084017 (2017).
- [57] F. Atamurotov, A. Abdujabbarov, and W.-B. Han, Effect of plasma on gravitational lensing by a Schwarzschild black hole immersed in perfect fluid dark matter, *Phys. Rev. D* **104**, 084015 (2021).
- [58] F. Atamurotov, A. Abdujabbarov, and J. Rayimbaev, Weak gravitational lensing Schwarzschild-MOG black hole in plasma, *Eur. Phys. J. C* **81**, 118 (2021).
- [59] Z. Turakhonov, F. Atamurotov, S. G. Ghosh, and A. Abdujabbarov, Probing effects of plasma on shadow and weak gravitational lensing by regular black holes in asymptotically safe gravity, *Phys. Dark Univ.* **48**, 101880 (2025).
- [60] R. Kumar, S. U. Islam, and S. G. Ghosh, Gravitational lensing by charged black hole in regularized 4D Einstein-Gauss-Bonnet gravity, *Eur. Phys. J. C* **80**, 1128 (2020), [arXiv:2004.12970 \[gr-qc\]](#).
- [61] R. Kumar Walia, Exploring nonlinear electrodynamics theories: Shadows of regular black holes and horizonless ultracompact objects, *Phys. Rev. D* **110**, 064058 (2024), [arXiv:2409.13290 \[gr-qc\]](#).
- [62] A. Bokulić, T. Jurić, and I. Smolić, Conundrum of regular black holes with nonlinear electromagnetic fields (2025), [arXiv:2510.23711 \[gr-qc\]](#).
- [63] H. Babaei-Aghbolagh, K. Babaei Velni, S. He, and F. Isapour, A Unified Causal Framework for Nonlinear Electrodynamics Black Hole from Courant-Hilbert Approach: Thermodynamics and Singularity (2025), [arXiv:2511.17407 \[hep-th\]](#).

- [64] A. Bokulić, T. Jurić, and I. Smolić, Nonlinear electromagnetic fields in strictly stationary spacetimes, *Phys. Rev. D* **105**, 024067 (2022), [arXiv:2111.10387 \[gr-qc\]](#).
- [65] A. Bokulić, I. Smolić, and T. Jurić, Constraints on singularity resolution by nonlinear electrodynamics, *Phys. Rev. D* **106**, 064020 (2022), [arXiv:2206.07064 \[gr-qc\]](#).
- [66] B. Toshmatov, Z. Stuchlík, and B. Ahmedov, Comment on “Construction of regular black holes in general relativity”, *Phys. Rev. D* **98**, 028501 (2018), [arXiv:1807.09502 \[gr-qc\]](#).
- [67] C. Moreno and O. Sarbach, Stability properties of black holes in selfgravitating nonlinear electrodynamics, *Phys. Rev. D* **67**, 024028 (2003), [arXiv:gr-qc/0208090](#).
- [68] K. Nomura, D. Yoshida, and J. Soda, Stability of magnetic black holes in general nonlinear electrodynamics, *Phys. Rev. D* **101**, 124026 (2020), [arXiv:2004.07560 \[gr-qc\]](#).
- [69] A. De Felice and S. Tsujikawa, Instability of Nonsingular Black Holes in Nonlinear Electrodynamics, *Phys. Rev. Lett.* **134**, 081401 (2025), [arXiv:2410.00314 \[gr-qc\]](#).
- [70] P. Niau Akmansoy and L. G. Medeiros, Constraining nonlinear corrections to Maxwell electrodynamics using $\gamma\gamma$ scattering, *Phys. Rev. D* **99**, 115005 (2019), [arXiv:1809.01296 \[hep-ph\]](#).
- [71] M. Fouché, R. Battesti, and C. Rizzo, Limits on nonlinear electrodynamics, *Phys. Rev. D* **93**, 093020 (2016), [Erratum: *Phys. Rev. D* **95**, 099902 (2017)], [arXiv:1605.04102 \[physics.optics\]](#).
- [72] P. A. Cano and Á. Murcia, Resolution of Reissner-Nordström singularities by higher-derivative corrections, *Class. Quant. Grav.* **38**, 075014 (2021), [arXiv:2006.15149 \[hep-th\]](#).
- [73] H. Maeda, Quest for realistic non-singular black-hole geometries: regular-center type, *JHEP* **2022** (11), 108, [arXiv:2107.04791 \[gr-qc\]](#).
- [74] E. L. B. Junior, J. T. S. S. Junior, F. S. N. Lobo, M. E. Rodrigues, L. F. D. da Silva, and H. A. Vieira, Dyonic regular black bounce solutions in general relativity, *Eur. Phys. J. C* **85**, 724 (2025), [arXiv:2502.13327 \[gr-qc\]](#).
- [75] G. W. Gibbons and M. C. Werner, Applications of the Gauss-Bonnet theorem to gravitational lensing, *Class. Quant. Grav.* **25**, 235009 (2008), [arXiv:0807.0854 \[gr-qc\]](#).
- [76] A. Ishihara, Y. Suzuki, T. Ono, T. Kitamura, and H. Asada, Gravitational bending angle of light for finite distance and the Gauss-Bonnet theorem, *Phys. Rev. D* **94**, 084015 (2016), [arXiv:1604.08308 \[gr-qc\]](#).
- [77] A. Ishihara, Y. Suzuki, T. Ono, and H. Asada, Finite-distance corrections to the gravitational bending angle of light in the strong deflection limit, *Phys. Rev. D* **95**, 044017 (2017), [arXiv:1612.04044 \[gr-qc\]](#).
- [78] W. Rindler and M. Ishak, Contribution of the cosmological constant to the relativistic bending of light revisited, *Phys. Rev. D* **76**, 043006 (2007), [arXiv:0709.2948 \[astro-ph\]](#).
- [79] I. Białynicki-Birula, *Quantum Theory of Particles and Fields: Birthday Volume Dedicated to Jan Łopuszański*, edited by B. Jancewicz and J. Lukierski (World Scientific, 1983) pp. 31–48.
- [80] Z. Li and T. Zhou, Equivalence of Gibbons-Werner method to geodesics method in the study of gravitational lensing, *Phys. Rev. D* **101**, 044043 (2020), [arXiv:1908.05592 \[gr-qc\]](#).